

X-ray diffraction tools for structural modeling of epitaxial films of an intrinsic antiferromagnetic topological insulator

Rafaela F. S. Penacchio, Yorí G. Camillo, and Sérgio L. Morelhão
Institute of Physics, University of São Paulo, 05508-090 São Paulo, SP, Brazil

Celso I. Fornari, Philipp Kagerer, Sebastian Buchberger, Hendrik Bentmann, and Friedrich Reinert
*Experimentelle Physik VII and Würzburg Dresden Cluster of Excellence ct.qmat,
 Fakultät für Physik und Astronomie, Universität Würzburg, Am Hubland, D-97074 Würzburg, Germany*

Martin Kamp
*Physikalisches Institut and Röntgen-Center for Complex Material Systems (RCCM),
 Fakultät für Physik und Astronomie, Universität Würzburg, Würzburg D-97074, Germany*

Synthesis of new materials demands structural analysis tools suited to the particularities of each system. Van der Waals (vdW) materials are fundamental in emerging technologies of spintronics and quantum information processing, in particular topological insulators and, more recently, materials that allow the phenomenological exploration of the combination of non-trivial electronic band topology and magnetism. Weak vdW forces between atomic layers give rise to composition fluctuations and structural disorder that are difficult to control even in a typical binary topological insulators such as Bi_2Te_3 . The addition of a third element as in MnBi_2Te_4 makes the epitaxy of these materials even more chaotic. In this work, statistical model structures of thin films on single crystal substrates are described. It allows the simulation of X-ray diffraction in disordered heterostructures, a necessary step towards controlling the epitaxial growth of these materials. On top of this, the diffraction simulation method described here can be readily applied as a general tool in the field of design new materials based on stacking of vdW bonded layers of distinct elements.

I. INTRODUCTION

Two-dimensional (2D) van der Waals (vdW) materials have experienced an explosive growth after graphene, and new families of 2D systems and block-layered bulk materials have been discovered [1–3]. The possibility of tuning their electronic properties via structural parameters make the layered vdW materials attractive from both fundamental and device engineering points of view. This field has become particularly interesting after the experimental discovery of three-dimensional (3D) topological insulators (TIs), having as a prototypical the bismuth chalcogenide compounds [4–7]. To control the chemical potential of these compounds without using extrinsic doping, growth methods and properties of thin films have been investigated [8–11]. However, the weakness of vdW interlayer forces lead in general to systems undergoing drastic changes as a function of subtle variation in growth conditions. Finding controllable fabrication processes of such systems has proven challenging [12, 13]. On top of this, the recently discovered intrinsic magnetic topological insulator MnBi_2Te_4 has added a new chapter to the phenomenological exploration of combining non-trivial electronic band topology and magnetism. Contrary to other attempts of breaking time-reversal symmetry by diluted doping of transition metals or rare-earth elements on 3D TIs [14–18], this material carries in its unit cell ordered layers of Mn atoms, providing a ferromagnetic ordering in the plane and a broad range of out-of-plane configurations depending on the stacking sequence [19, 20]. This compound is part

of the $(\text{MnBi}_2\text{Te}_4)_n(\text{Bi}_2\text{Te}_3)_m$ homologous series, similar to the $(\text{Bi}_2\text{Te}_3)_n(\text{Bi}_2)_m$ series [21–23]. The series is composed by stacking two fundamental building blocks and spans from Bi_2Te_3 ($n = 0$), the archetypal of 3D TI without magnetic ordering, to the intrinsic antiferromagnetic MnBi_2Te_4 ($m = 0$), passing through an infinity of intermediary phases [24–26].

For the 3D non-magnetic TI, Bi_2Te_3 , the unit cell is composed by stacking three quintuple layers (QLs). These QLs are fundamental building blocks always started and terminated in Te atoms as Te-Bi-Te-Bi-Te. The Te-Bi atoms are ionic bonded inside the QLs, while these blocks are coupled together along the [0001] direction due to weak vdW forces between the Te atoms in adjacent blocks. By inserting Mn in this structure, an extra MnTe double layer is formed inside the QL, leading to the existence of septuple layers (SLs) as Te-Bi-Te-Mn-Te-Bi-Te. The atomic Mn layer inside the SLs present a net out-of-plane magnetic moment, that is, the neighbor atoms are ferromagnetically coupled inside the layer. When stacked together, the SLs present anti-ferromagnetic (AFM). The intermediary phases are determined by the ratio of SLs and QLs, and present interesting AFM properties [27]. Besides the above mentioned magnetic properties of this series, an even richer interplay between topology and magnetism is expected in the 2D regime when reducing the number of stacked layers [1]. Such properties make this intrinsic magnetic TI highly attractive. However, a great challenge rising in this field is to control and understand the growth mechanisms of this compound in order to suppress the formation of structural defects and prepare perfectly ordered

layers to explore the 3D to 2D transition.

Simulations of X-ray scattering and diffraction are well-established procedures for structural analysis at nanometer and subnanometer length scales of layered materials, ranging from amorphous films to crystalline ones such as epitaxial layers on single-crystal substrates [28, 29]. Higher are the ordering in stacking sequences of the atomic layers, the more pronounced are the diffracted intensities at higher angles allowing more refined structure models. X-ray theories are well comfortable at the limiting cases, either amorphous films or perfect periodic layer sequences, that is crystalline films. However, in developing new materials and processing technologies, layered materials with random layer sequences of large d -spacing can often be found. Combined with the very high dynamical range of advanced X-ray sources and instruments, this kind of material represent a challenging in theoretical approach for X-ray diffraction simulation [30, 31]. By using state-of-the-art X-ray diffraction simulation applied to the $(\text{Bi}_2\text{Te}_3)_m(\text{MnBi}_2\text{Te}_4)_n$ homologous series, it is possible to study details of the stacking layers, providing information to further improvements on the growth of this material.

In this work, we describe how to adapt a general recursive equation for simulating X-ray dynamical diffraction in layered materials to the case of thin films of $\text{Mn}_x\text{Bi}_2\text{Te}_{3+x}$ (MBT) grown by molecular beam epitaxy on BaF_2 (111) substrates. The films are stacks of n vdW bounded MnBi_2Te_4 septuple layers where the occurrence of m Bi_2Te_3 quintuple layers leads to films of composition $x = n/(n + m)$. Interface quality, random stacking sequences, surface finishing, and evolution of defects during growth are accessible parameters by curve fitting with the recursive equation. The effectiveness of this approach is demonstrated for analysing X-ray diffraction in films with different compositions and disorder parameter, ranging from random to perfect periodic stacking sequences of atomic layers.

II. STRUCTURE MODELS

A key point in vdW epitaxy is the weakness of interlayer forces. It favours, in principle, flexibilization of the lateral lattice matching requirements [32, 33] at the same time that makes challenging the control of film composition and other lattice defects [12, 34–36]. Modeling disordered heterostructures is a necessary step towards general procedures for structural analysis of materials based on vdW epitaxy. Composition fluctuation is related to the occurrence of distinct building blocks—sets of atomic monolayers sharing covalent bonds—randomly stacked along film thickness and bonded to each other by weak vdW forces. Figures 1a and 1b show the building blocks that have been used for modeling $\text{Bi}_2\text{Te}_{3-\delta}$ films with deficit δ of tellurium [29], and in Figures 1d 1c, the blocks that are used here for modeling the MBT films.

Accounting for differences in the general appearance

of the films with composition fluctuation can be accomplished by correctly choosing a probability function to control the stacking sequences of two building blocks; the main block labeled A and the secondary one labeled B . For instance, in one case both types of building blocks can occur adjacently to each, as in the sequence $A:A:B:B:A:A:A:B:A$, and in the other case it occurs to one type of block only, as in $A:A:B:A:A:A:B:A:A$. Even in cases where the synthesis is aimed at obtaining materials with only the main block A , it is necessary to know how to evidence and quantify, if possible, the occurrence of the other block, block B , that is responsible for composition fluctuation. In more refined models, changes in interlayer distances as a function of composition can be taken into account, as in the case of $\text{Bi}_2\text{Te}_{3-\delta}$ films [22, 23]. However, in new materials as the MBT epitaxial films [25], further improvement in film quality will be necessary before resolving the variations in interlayer distances with composition.

In structure models, a stack of N adjacent A blocks—without a B block in the middle—occurs with probability

$$P(N) = \int_{N-1/2}^{N+1/2} p(z) dz \quad (1)$$

where N stands for non-negative integers. Therefore, films made exclusively of A blocks have $P(N) = 1$ for N as the total number of blocks in the film structure along the growth direction. To account for films where the secondary B blocks can be adjacent to A blocks only, the probability function based on a standard log-normal function

$$p(z) = \frac{1}{z \sigma_L \sqrt{2\pi}} e^{-\frac{1}{2} \left[\frac{\ln(z) - \ln(b)}{\sigma_L} \right]^2}, \quad (2)$$

can describe well the stacking sequences from totally disordered to a perfectly periodic heterostructure. $b = N_0 \exp(\sigma_L^2)$, N_0 is the mode, and σ_L the standard deviation in log-scale. To assure that there will be no $B:B$ sequences in the films, that is $P(0) = 0$, the small value of $p(z)$ in the range from $z = 0$ to $1/2$ is accounted for in $P(1) = \int_0^{3/2} p(z) dz$. The closest two B blocks can be to each other is in $B:A:B$, which occurs with probability $P(1)$.

Examples of periodic and disordered sequences are shown in Figure 2. For a mode $N_0 = 2$ and a narrow deviation such as $\sigma_L = 0.2$, the distribution of probability in Figure 2a gives about 5% for isolated A , 77% for $A:A$, and 18% for $A:A:A$. The chances for generating a highly periodic $A_n B_m$ heterostructure is given by $P(N_0)^{n/N_0}$, as the 12:6 ($n:m$) film in Figure 2e with stacking sequence $A:A:B:A:A:B:A:A:B:A:A:B:A:A:B$ that occurs with probability $P(2)^6 \simeq 20\%$ within an ensemble of structure models. Perfectly periodic heterostructures also require $N_0 = n/m$ to be an integer number. On the other hand, when a broad probability function is used for structure models generation, such as the one with $\sigma_L = 0.6$ in Figure 2b, disordered heterostructures are highly probable, as in Figure 2f with sequence

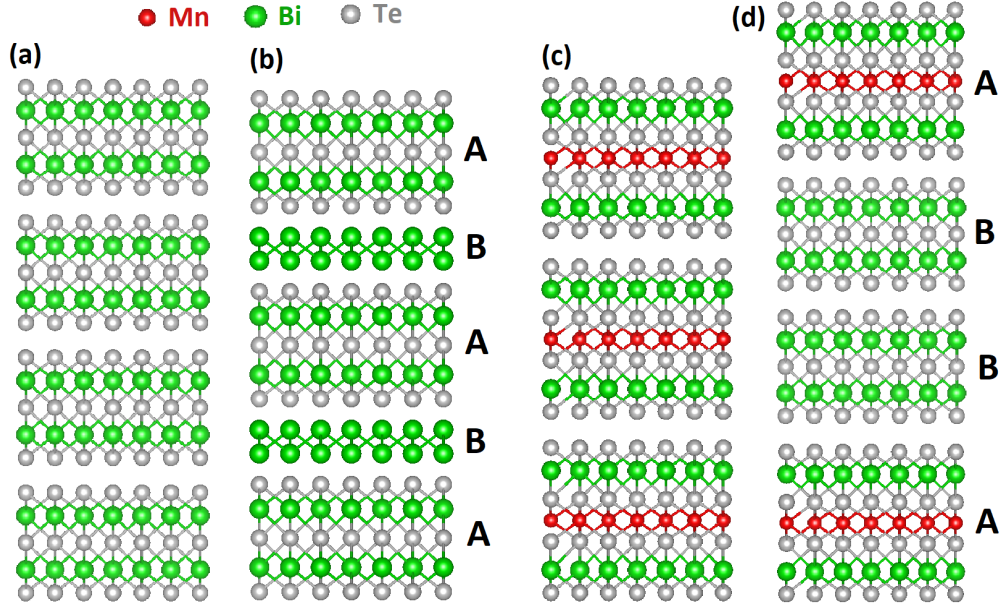


FIG. 1. Building blocks in $\text{Bi}_2\text{Te}_{3-\delta}$ and MBT epitaxial films. (a) Pure Bi_2Te_3 phase with no Te deficit ($\delta = 0$). (b) Bilayers of bismuth as in $(\text{Bi}_2\text{Te}_3)_n(\text{Bi}_2)_m = A_nB_m$ lead to films with Te deficit $\delta = 3m/(n + m)$; main and secondary building blocks: $A = \text{Te}:\text{Bi}:\text{Te}:\text{Bi}:\text{Te}$ and $B = \text{Bi}:\text{Bi}$. (c) Single MnBi_2Te_4 phase. (d) Mixing of phases $(\text{MnBi}_2\text{Te}_4)_n(\text{Bi}_2\text{Te}_3)_m = A_nB_m$ lead to $\text{Mn}_x\text{Bi}_2\text{Te}_{3+x}$ films with composition $x = n/(n + m)$ or Mn deficit $\gamma = 1 - x = m/(n + m)$; main and secondary building blocks: $A = \text{Te}:\text{Bi}:\text{Te}:\text{Mn}:\text{Te}:\text{Bi}:\text{Te}$ and $B = \text{Te}:\text{Bi}:\text{Te}:\text{Bi}:\text{Te}$.

$A:A:A:B:A:B:A:B:A:B:A:A:A:A:A:B:A:B$. Despite the degree of disorder, there is no $B:B$ sequences as the probability function was chosen to provide $P(0) = 0$. This probability function with $p(z)$ in eq. (2) has been used for modeling $\text{Bi}_2\text{Te}_{3-\delta}$ films, as detailed described elsewhere [29].

In epitaxial films where both types of building blocks can form stacks of equal blocks, that is where B blocks can appear adjacently to each other, the probability function has to allow $P(0) > 0$. It can be accomplished by using, for instance, a Gaussian-based function such as

$$p(z) = \frac{e^{-\frac{1}{2}\left(\frac{z-N_0}{\sigma_G}\right)^2}}{\int_{-1/2}^{\infty} e^{-\frac{1}{2}\left(\frac{z-N_0}{\sigma_G}\right)^2} dz} \quad (3)$$

with mode N_0 and standard deviation σ_G . Narrow probability functions, as in Figure 2c where $P(0) \approx 0$, lead to more ordered distribution of the B blocks, as in the sequence $A:B:A:A:A:B:A:A:A:B:A:B:A:A:A:B:A:B:A$ shown in Figure 2g. However, broader probability functions, as in Figure 2d, increase the disorder of the B blocks and also the probability of some of them to appear together as in the sequence $A:A:A:B:B:A:A:A:A:B:B:A:A:A:A:A:B:A:B$ graphically represented in Figure 2h.

III. X-RAY DIFFRACTION SIMULATION

For a given probability function and film composition, hundreds of structure models are generated with constant numbers of both A and B blocks, as exemplified in Figure 3. Such ensemble of models represents possible statistical fluctuation within film domains distributed over the sample area. X-ray reflectivity of each model is calculated by adding up reflection and transmission coefficients of the successive layers along film thickness. If $r_{X,Y}$ and $t_{X,Y}$ stand for reflection and transmission coefficients of generic X and Y layers, the coefficients of the combined $Y:X$ layer with X on top of layer Y are calculated according to [29]

$$\begin{aligned} r_{YX} &= r_X + r_Y \frac{t_X t_X e^{2i\varphi}}{1 - \bar{r}_X r_Y e^{2i\varphi}}, \\ \bar{r}_{YX} &= \bar{r}_Y + \bar{r}_X \frac{t_Y t_Y e^{2i\varphi}}{1 - \bar{r}_X r_Y e^{2i\varphi}}, \quad \text{and} \\ t_{YX} &= \frac{t_X t_Y e^{i\varphi}}{1 - \bar{r}_X r_Y e^{2i\varphi}}. \end{aligned} \quad (4)$$

$\varphi = -\frac{1}{2}Qd$ is the phase delay every time the X-ray wave of wavelength λ crosses the interlayer distance d between the X and Y layers, and $Q = (4\pi/\lambda) \sin \theta$ is the modulus of the scattering vector perpendicular to film thickness for an incidence angle θ . In general, reflection coefficients are different when the X-ray impinges from the top, coefficients r_X , r_Y , and r_{YX} , or from the bottom, coefficients \bar{r}_X , \bar{r}_Y , and \bar{r}_{YX} .

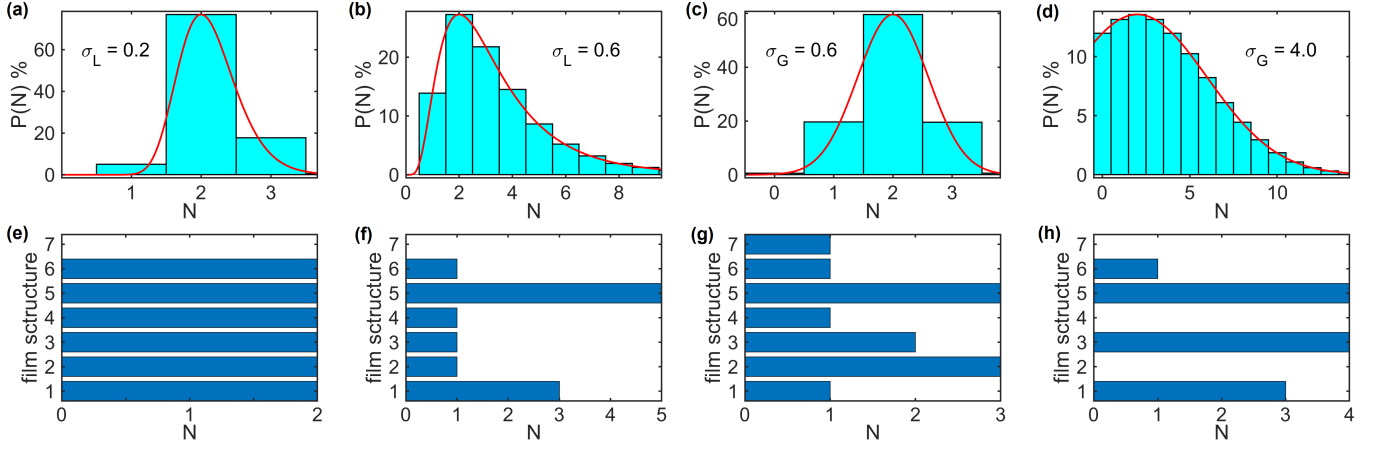


FIG. 2. (a-d) Probability functions $P(N)$, eq. (1), for stacking sequences of N adjacent A blocks interleaved by B blocks. (e-h) Graphic schemes of $A_{12}B_6$ film structures along thickness according to the probability showed above each scheme: stacks of N adjacent A blocks (blue bars) separated by B block (vertical gap in between the blue bars). (h) Disordered structure with adjacent B blocks (large vertical gap). $P(0)$ gives the probability for the absence of one A block in between two B blocks.

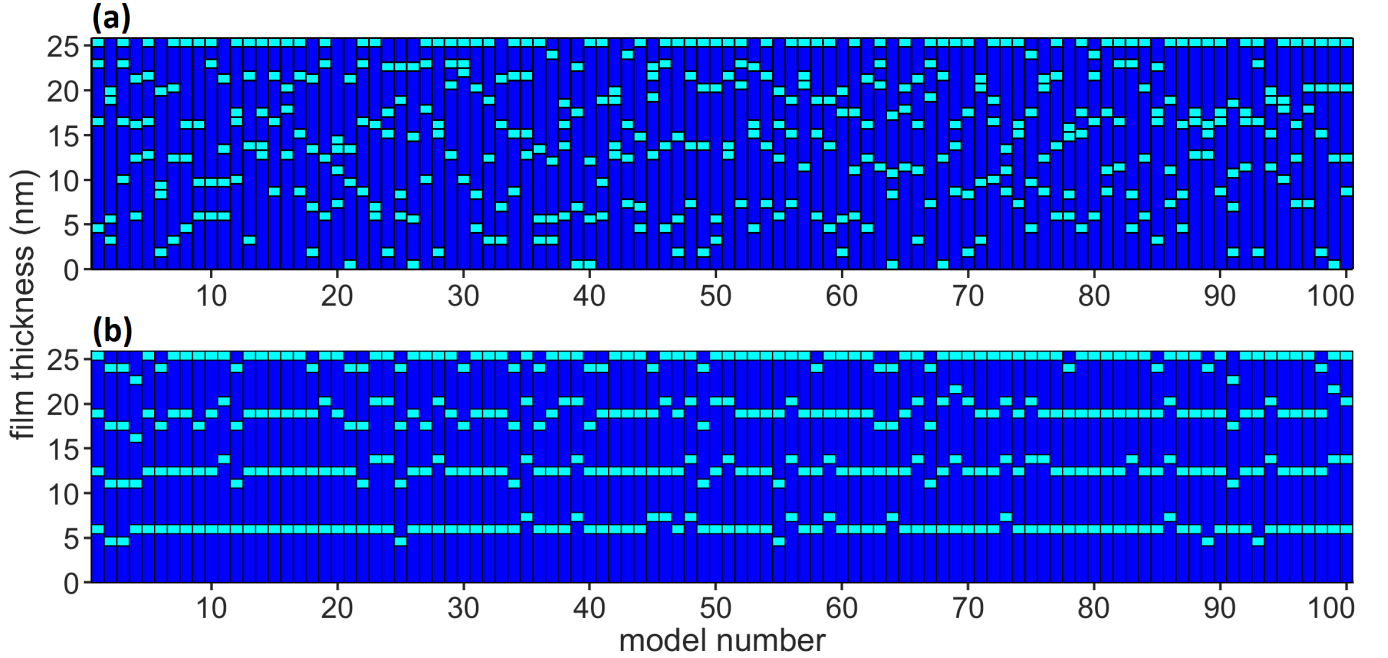


FIG. 3. Ensembles of hundred structure models for $A_{16}B_4$ films where $A = \text{MnBi}_2\text{Te}_4$ (blue, 1.36 nm) and $B = \text{Bi}_2\text{Te}_3$ (cyan, 1.02 nm). (a) $\sigma_G = 4$ and (b) $\sigma_G = 0.4$ in eq. (3). Total film thickness is 25.8 nm for all models.

Eqs. (4) are used recursively, starting from the atomic monolayers within the building blocks A and B , whose interlayer distances are given in Table I. For an atomic monolayer, $r_X = \bar{r}_X = -i\Gamma \sum_a \eta_a f_a(Q, E)$ and $t_X = 1 + i\Gamma \sum_a \eta_a f_a(0, E)$ where η_a is the area density of atoms a in the monolayer plane and $f_a(Q, E) = f_a^0(Q) + f_a'(E) + i f_a''(E)$ are their atomic scattering factors with resonant amplitudes for X-ray photons of energy E , see section S3 in the Support Information. The parameter $\Gamma = r_e \lambda C / \sin \theta$ arises from the scattering and photoelectric absorption cross sections, and it is very small due to

the value of electron radius $r_e = 2.818 \times 10^{-5} \text{ \AA}$. The $\sin \theta$ takes into account area variation of the beam footprint at the sample surface, and the polarization term C is always equal to 1 for t_X , as well as in r_X when using linearly polarized X-rays (most synchrotron facilities) [37]. For accurate curve fitting purposes with unpolarized X-rays, take $C^2 = \frac{1}{2}(1 + \cos^2 2\theta)$ in r_X . Throughout this work, $C = 1$ is considered for sake of simplicity.

After calculating the reflection coefficients r_A and r_B of the A and B building blocks, the reflection coefficients of any sequence of blocks such as $A : A : B : A : A : B$

TABLE I. Atomic monolayers (MLs) distances d in structure models of MBT films on BaF_2 (111) substrate. Building block $A = \text{Te(1)-Bi(1)-Te(2)-Mn(1)-Te(3)-Bi(2)-Te(4)}$ and $B = \text{Te(1)-Bi(1)-Te(2)-Bi(2)-Te(3)}$. Substrate MLs along [111] direction: F(1)-Ba(1)-F(2) , distances $d_{\text{BaF}} = 0.08949 \text{ nm}$ and $d_{\text{FF}} = 0.17898 \text{ nm}$. In-plane lattice parameters: $a_A = 0.4334 \text{ nm}$, $a_B = 0.4386 \text{ nm}$, and $a_S = 0.4384 \text{ nm}$. All d -values are from bulk [38, 39].

building block A (MnBi_2Te_4)		building block B (Bi_2Te_3)	
MLs	d (nm)	MLs	d (nm)
Te(1)-Bi(1) and Bi(2)-Te(4)	0.17073	Te(1)-Bi(1) and Bi(2)-Te(3)	0.17434
Bi(1)-Te(2) and Te(3)-Bi(2)	0.21532	Bi(1)-Te(2) and Te(2)-Bi(2)	0.20331
Te(2)-Mn(1) and Mn(1)-Te(3)	0.15928	Te(3):Te(1) ($B:B$ vdW gap)	0.26126
Te(4):Te(1) ($A:A$ vdW gap)	0.27301	Te(1)-Te(1) $\rightarrow d_{QL}$	1.01656
Te(1)-Te(1) $\rightarrow d_{SL}$	1.36367	—	—

follows straightforward from eqs. (4), that is

$$\begin{aligned}
 (X=A, Y=A) &\rightarrow r_{AA}, \\
 (X=B, Y=AA) &\rightarrow r_{AAB}, \quad \text{and} \\
 (X=AAB, Y=AAB) &\rightarrow r_{AABAAB}. \quad (5)
 \end{aligned}$$

The $A:A$ and $B:B$ vdW gap distances are given in Table I, and the mean value of 0.26713 nm has been used for the $A:B$ vdW gap. In most cases, it is necessary to consider the presence of the perfect and thick substrate lattice underneath the film. As detailed elsewhere [29], eqs. (4) also provides the dynamical diffraction solution in specular reflection geometry where refraction, rescattering, and photoelectric absorption are taken into account—the impact of rescattering on diffracted intensities can be figured out by suppressing the term $\bar{r}_X r_Y e^{2i\varphi}$ in the denominator of the coefficients in eqs. (4). The reflection coefficient r_S , obtained from eqs. (4), for a thick substrate can be included when simulating the X-ray reflectivity curve $R(\theta)$ for a given model by repeating one more step of the recursive procedure, that is $(X = AABAAB, Y = S) \rightarrow r_{SAABAAB}$. It provides $R(\theta) = |r_{SAABAAB}|^2$ as the reflectivity curve of the particular example of model in eq. (5) grown on top of a single crystal substrate.

IV. MATERIALS AND METHODS

Thin films of $(\text{MnBi}_2\text{Te}_4)_n(\text{Bi}_2\text{Te}_3)_m$ were grown on freshly cleaved BaF_2 (111) substrates using effusion cells charged with Bi_2Te_3 and phase pure MnTe as prepared by inorganic solid-state reactions [42]. The beam equivalent pressure (BEP) is monitored by an ion gauge before and after each growth. The manganese supply is defined by the ratio of the BEPs as $\Phi_{\text{Mn}} = \text{BEP}_{\text{MnTe}}/\text{BEP}_{\text{Bi}_2\text{Te}_3}$. During deposition, the background pressure stays below $5 \times 10^{-8} \text{ mbar}$, against $7 \times 10^{-11} \text{ mbar}$ base pressure of the growth chamber. BaF_2 substrates were pre-heated at 350°C for 10 min before starting deposition, and kept at 280°C during deposition. All samples were prepared with a fixed $\text{BEP}_{\text{Bi}_2\text{Te}_3}$, resulting in a deposition rate of 0.02 \AA/s for the Bi_2Te_3 cell. The Mn supply controlled

through the MnTe effusion cell, providing $\Phi_{\text{Mn}} = 0.06$, 0.07 , and 0.11 for samples labelled S60, S57, and S62, respectively. These samples were covered with a 80 nm thick Te capping layer to avoid surface oxidation. Another set of samples, without the Te cap, was prepared within similar conditions: samples S27, S34, and S29 with $\Phi_{\text{Mn}} = 0.075$, 0.086 , and 0.102 , respectively. For sample S34, the substrate temperature was kept at 300°C during deposition. Nominal thickness of the films is close to 20 nm , except in sample S57 where it is closer to 40 nm .

XRD measurements were performed with a Bruker high resolution X-ray diffractometer equipped with Göbel mirror, Ge (220) monochromator, and $\text{CuK}_{\alpha 1}$ radiation ($\lambda = 1.540562 \text{ \AA}$). Transmission electron microscopy (TEM) samples were prepared at the Wilhelm Conrad Röntgen Research Center for Complex Material System (RCCM) by using Ga^+ ion beam milling. Imaging was performed using an uncorrected FEI Titan 80–300 TEM.

V. RESULTS AND DISCUSSIONS

Experimental and simulated long-range Q -scans along the surface normal direction are shown in Figure 4. Diffraction peaks of epitaxial MBT films are clearly identified by comparing with the simulated ones. Traces of Bi_2Te_3 layers are seen in sample S57 (arrows) near peaks $L9$ and $L21$ of the MBT film. Besides film and substrate reflections, there are also diffraction peaks of 010 , 020 , and 030 reflections from the protective Te capping layer, and two diffraction peaks from a MnTe phase in the S62 sample film grown under higher Mn supply. The presence of MnTe layers epitaxially oriented with the substrate lattice have already been observed, as well as the formation of multiple MnTe layers inside the MnBi_2Te_4 blocks, given rise to blocks composed of 9, 11 or 13 layers [43]. The presence of MnTe clusters perturb locally the magnetic order of the sample and must be avoided.

Figure 5 shows Q -scans for the samples without the Te capping layer. No signal from the 002 MnTe reflection can be identified at the right side of the MBT $L12$

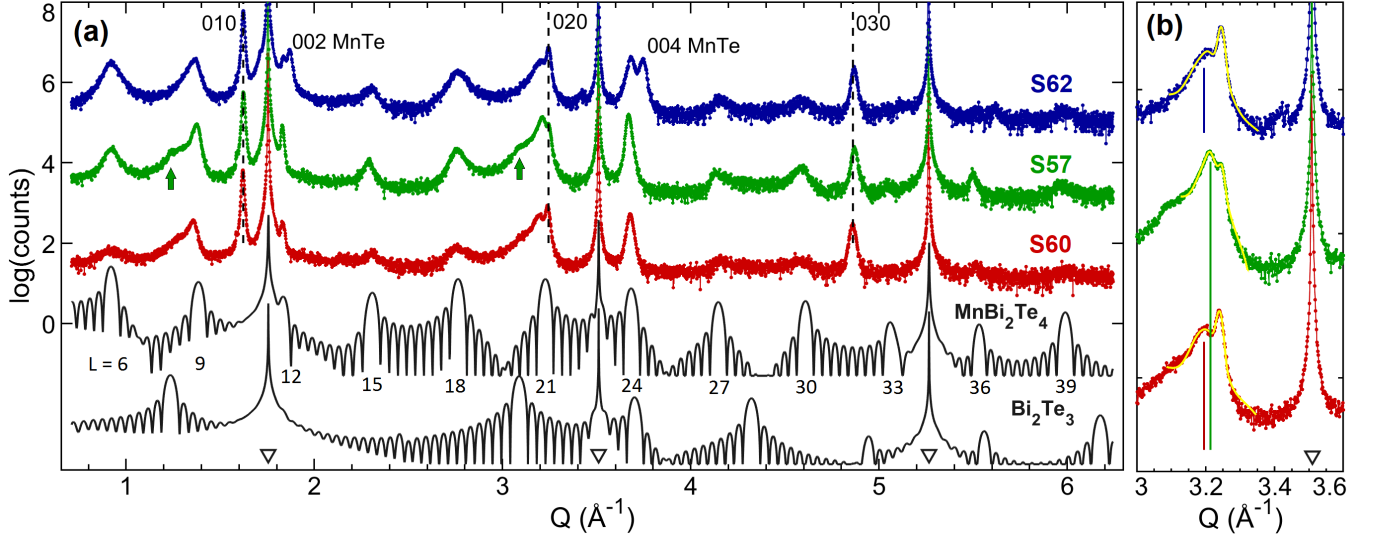


FIG. 4. (a) Q -scans along the surface normal direction in epitaxial MBT films on BaF_2 (111) substrate. $Q = (4\pi/\lambda) \sin \theta$. Sample labels (see § Materials and Methods) are indicated aside each experimental scan. Sharp-high intensity peaks (down triangles) stand for 111, 222, and 333 reflections of the substrate lattice. The 010, 020, and 030 reflections (dashed lines) from a hexagonal Te phase [40] are originated by the Te protective capping layer, while the 002 and 004 reflection indexes refer to a hexagonal MnTe phase [41] observed in the sample S62 only. Broad peaks are $00L$ reflections ($L = 6, 9, \dots, 39$) from MBT films. Contributions from Bi_2Te_3 layers are pointed out by arrows. Simulated curves for MBT and Bi_2Te_3 single phase 13 nm thick films are shown at the bottom (out of vertical scale) as reference for peak positions. (b) Zooming of experimental profiles around film L_{21} peak and substrate 222 reflection. Q positions (vertical lines) of the L_{21} peaks obtained by line profile fitting (yellow lines) are indicated: $Q_{21}^{\text{S60}} = 3.201 \text{ \AA}^{-1}$, $Q_{21}^{\text{S57}} = 3.214 \text{ \AA}^{-1}$, and $Q_{21}^{\text{S62}} = 3.208 \text{ \AA}^{-1}$ for samples S60, S57, and S62, respectively.

peak, even in the case of sample S29 with Mn supply $\Phi_{\text{Mn}} = 0.102$ that is close to $\Phi_{\text{Mn}} = 0.11$ used for preparing sample S62 (Figure 4). However, there are other features evidenced in these intensity curves. As the Mn supply increases, peak L_6 becomes narrower and peak L_9 moves slightly towards the expected position of the pure phase. By fitting the line profile of peak L_6 with two gaussians, they appears set apart by $\Delta Q = 0.15 \text{ \AA}^{-1}$ and 0.10 \AA^{-1} in the samples for which $\Phi_{\text{Mn}} = 0.075$ and 0.086 , respectively. In the sample for which $\Phi_{\text{Mn}} = 0.102$, no separation of the gaussians is detected. To clearly understand such features, XRD simulation becomes crucial. Structure models of MBT films based on two building blocks, as depicted in Figure 1d, are supported by TEM images as the one in Figure 6 where only MnBi_2Te_4 septuple layers (SLs) and Bi_2Te_3 quintuple layers (QLs) have been observed [25]. Bismuth bilayers owing to the deficit of tellurium have been suppressed, probably due to the extra amount of Te from the MnTe source.

Simulated Q -scans in disordered $(\text{MnBi}_2\text{Te}_4)_n(\text{Bi}_2\text{Te}_3)_m$ films as a function of the Mn deficit $\gamma = m/(n+m)$ are shown in Figure 7; low Q regions are detailed in section S1 of the Support Information. For a given degree of disorder, the simulated curves reveal that well visible diffraction peaks as L_6 and L_{18} undergo a splitting into two superlattice satellite peaks set apart by a ΔQ value nearly proportional to the content of QLs (Bi_2Te_3 blocks) or Mn deficit. Most satellite peaks

vanish as the disorder parameter σ_G increases, as better seen in Figure 8. But, the splitting of the L_6 and L_{18} peaks remain measurable even in films where the QLs are distributed with high degree of disorder. Within the approximation of stable interlayer distances summarized in Table I, the films have thickness $T = n d_{\text{SL}} + m d_{\text{QL}}$, and mean superlattice period $\langle D \rangle = T/m$ where $d_{\text{SL}} = 1.36367 \text{ nm}$ and $d_{\text{QL}} = 1.01656 \text{ nm}$ (Table I). It provides satellite reflections set apart by

$$\begin{aligned} \Delta Q(\gamma) &= \frac{2\pi}{\langle D \rangle} = \frac{2\pi m}{n d_{\text{SL}} + m d_{\text{QL}}} = \\ &= \frac{2\pi \gamma}{d_{\text{SL}} - \gamma(d_{\text{SL}} - d_{\text{QL}})} \approx \frac{2\pi}{d_{\text{SL}}} \gamma. \end{aligned} \quad (6)$$

The Mn deficit γ also shifts the L_{21} peak position. In MnBi_2Te_4 film, the lattice parameter $c = 3d_{\text{SL}}$, $Q = 2\pi L/c$, and hence for $L = 21$, $Q_{21} = 2\pi/\langle d \rangle_0$ as $\langle d \rangle_0 = d_{\text{SL}}/7$. In the case of $(\text{MnBi}_2\text{Te}_4)_n(\text{Bi}_2\text{Te}_3)_m$ films, the mean atomic interlayer distance is $\langle d \rangle = T/(7n + 5m)$ where $7n + 5m$ corresponds to the total number of atomic monolayers stacked along the film thickness. It leads to

$$\begin{aligned} Q_{21}(\gamma) &= \frac{2\pi}{\langle d \rangle} = \frac{2\pi(7 - 2\gamma)}{d_{\text{SL}} - \gamma(d_{\text{SL}} - d_{\text{QL}})} = \\ &\approx \frac{2\pi}{\langle d \rangle_0} + \frac{2\pi}{\langle d \rangle_0} \left(\frac{5}{7} - \frac{d_{\text{QL}}}{d_{\text{SL}}} \right) \gamma. \end{aligned} \quad (7)$$

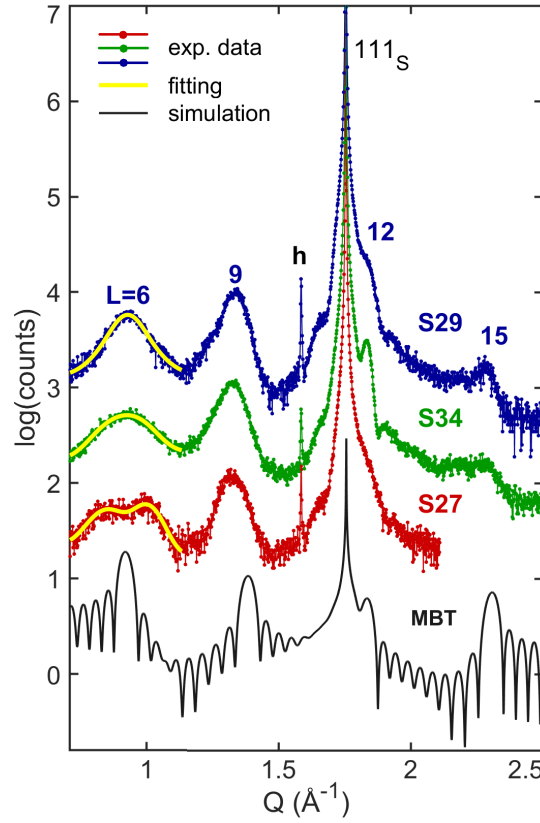


FIG. 5. Q -scans along the surface normal direction in epitaxial MBT films on BaF_2 (111) substrate. $Q = (4\pi/\lambda) \sin \theta$. Sample labels (see § Materials and Methods) are indicated aside each experimental scan (lines with dots). Film $00L$ reflections with $L = 6, 9, 12$, and 15 are visible, as well as the 111 substrate reflection. Simulated curve for a 13 nm thick MBT film is shown at the bottom (out of vertical scale) as reference for peak positions. A hybrid reflection is seen on all scans (letter h); it is a substrate/film reescattering phenomenon extensively discussed elsewhere [44]. Line profile fitting (yellow lines) by two gaussians of the diffraction peak L6 provide splitting values of $\Delta Q = 0.15 \text{ \AA}^{-1}$, 0.10 \AA^{-1} , and null for samples S27, S34, and S29, respectively.

The linear behaviour of ΔQ and Q_{21} as function of γ are shown in Figure 9. For small Mn deficit ($\gamma \lesssim 0.25$), the splitting can be taken as $\Delta Q \approx 0.46 \gamma [\text{\AA}^{-1}]$, while the shift in the $L21$ peak position is $\Delta Q_{21}(\gamma) = Q_{21}(\gamma) - 2\pi/\langle d \rangle_0 \approx -0.10 \gamma [\text{\AA}^{-1}]$.

By using the substrate 222 reflection at $Q = 3.5105(\pm 0.0001) \text{ \AA}^{-1}$ as reference, the expected $L21$ peak position is at $Q_{21}(0) = 2\pi/\langle d \rangle_0 = 3.2253 \text{ \AA}^{-1}$ for unstrained non-tilted epitaxial films with no Mn deficit. In Figure 4b, the experimental $L21$ peaks have been observed at slightly different positions, implying in $\Delta Q_{21}^{S60} = Q_{21}^{S60} - Q_{21}(0) = -0.027 \text{ \AA}^{-1}$, $\Delta Q_{21}^{S57} = -0.014 \text{ \AA}^{-1}$, and $\Delta Q_{21}^{S62} = -0.020 \text{ \AA}^{-1}$. According to eq. (7), the analyzed films have compositions $x = 0.73, 0.86$, and 0.80 , respectively. However, these values are reliable as far as the interlayer distances have no dependence with composition, disorder, and film thickness. In highly disordered heterostructures, peak broadening is observed instead of peak splitting into superlattice satellite peaks. The X-ray reflectivity simulations in Figures 7

and 8 clearly show that peaks susceptible to composition are much broader than other peaks, such as the $L24$ peak that has presented a nearly constant width as a function of composition and heterostructure disorder. Therefore, $L6$ peak significantly broader than $L24$ peak can be taken as another evidence, although qualitative, of Mn deficit and disorder in the films. For the sake of comparison, the $L6$ peaks in the S60, S57, and S62 samples have width (fwhm) around $w_{L6} \approx 0.067 \text{ \AA}^{-1}$, against nearly half of this value for the $L24$ peak.

Invariance of $L24$ peak width with composition and disorder implies that their widths $w_{24}^{S60} = 0.0315 \text{ \AA}^{-1}$, $w_{24}^{S57} = 0.0260 \text{ \AA}^{-1}$, and $w_{24}^{S62} = 0.0386 \text{ \AA}^{-1}$ from the experimental Q -scans, Figure 4a, can be used as a measure of the longitudinal (along film thickness) coherence lengths of $20.0(\pm 1.0) \text{ nm}$, $24.2(\pm 1.2) \text{ nm}$, and $16.3(\pm 0.7) \text{ nm}$, respectively. For samples S60 and S62, these lengths are close to the nominal thickness of 20 nm . But for sample S57, the coherence length is smaller than the nominal thickness of 40 nm , probably indicating to structural defects unaccounted for in the X-ray diffrac-

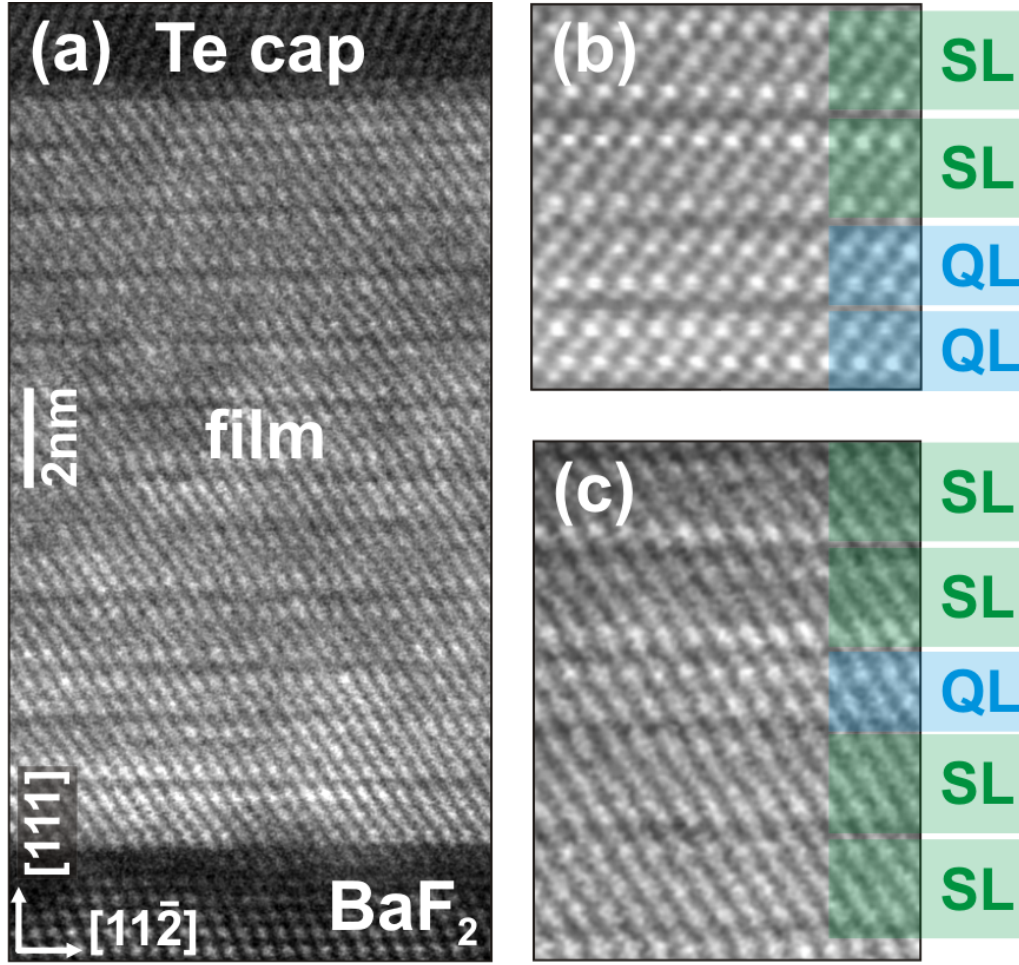


FIG. 6. Scanning transmission electron microscopy cross-sectional images of a 15 nm thick MBT film capped with Te. (a) Cross-sectional overview image showing the BaF_2 substrate, the epitaxial film, and the Te protective capping layer. (b,c) Detailed views of the film structure showing the coexistence of septuple layers (SLs) and quintuple layers (QLs).

tion simulation. Main peaks of the Bi_2Te_3 phase are clearly observed in the Q -scan of sample S57, as pointed out by arrows in Figure 4a. It means that segregation of phases has occurred in this film, which can in part justify a longitudinal coherence length smaller than the total film thickness and also corroborate to MBT phase with composition closer to $x = 1$.

Although vdW epitaxy can take place on substrates with relatively large lateral lattice mismatch [11, 45–47], it has been demonstrated in $\text{Bi}_2\text{Te}_3(001)$ films on $\text{BaF}_2(111)$ that even mismatch as small as 0.02% can drastically impact the lateral lattice coherence length, or the lateral size of crystalline domains [12]. In $\text{MnBi}_2\text{Te}_4(001)$ films on $\text{BaF}_2(111)$ the lattice mismatch $|\Delta a/a| = |a_A - a_s|/a_s$ is much bigger, of about 1.1%. If the amount ε of lattice misfit that can be elastically accommodated remains within the same order of magnitude, around 5×10^{-3} as observed in Bi_2Te_3 films, the lateral coherence length in MnBi_2Te_4 films is probably smaller than 27 nm ($\approx \frac{a_s}{\varepsilon + |\Delta a/a|}$) [12]. An indirect evidence of shorter in-plane coherence length is the absence of thickness fringes

around peak $L24$, as smaller domains can lead to more irregular film surfaces smearing out the fringes. The necessary thickness fluctuation for eliminating fringes around the $L24$ peak is discussed in section S2 of the Supporting Information.

In the case of samples S27, S34, and S29 with exposed films—no cap layers—, the splitting of peak $L6$ in two superlattice peaks as a function of the Mn supply is better evidenced, Figure 5. By using eq. (6) and the measured values of ΔQ , the Te deficit of $\gamma = 0.30$ and 0.21 are obtained for samples S27 ($\Phi_{\text{Mn}} = 0.075$) and S34 ($\Phi_{\text{Mn}} = 0.086$), respectively. Both sets of samples, the capped and not capped ones, are indicating that to prevent the formation of undesired MnTe layers by limiting the Mn supply to about $\Phi_{\text{Mn}} = 0.1$, films with composition close to $\text{Mn}_{0.8}\text{Bi}_2\text{Te}_{3.8}$ are obtained. This value of $x \simeq 0.8$ also corresponds to a limit value of composition detection capability by X-ray diffraction regarding the actual quality of the epitaxial MBT films.

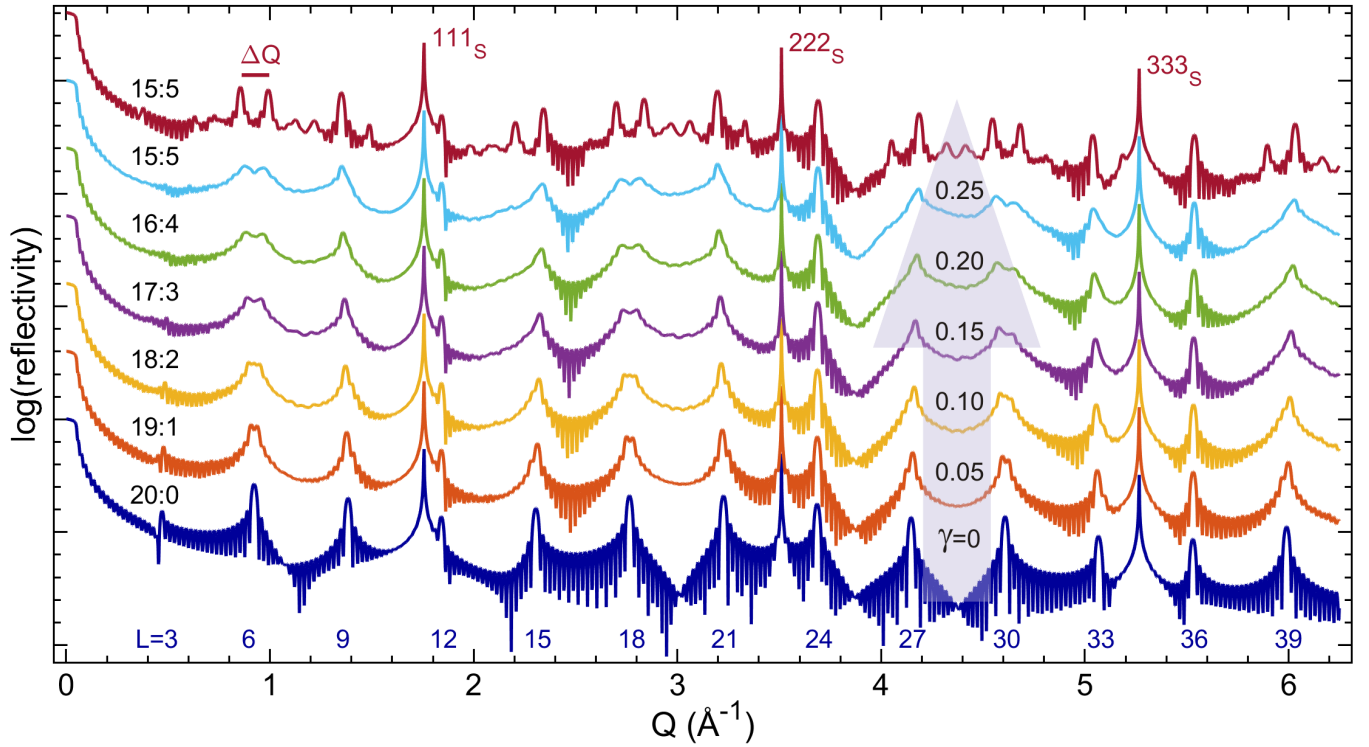


FIG. 7. Simulated Q -scans in epitaxial $(\text{MnBi}_2\text{Te}_4)_n(\text{Bi}_2\text{Te}_3)_m$ films on BaF_2 (111) substrate as a function of composition $n:m$. Structure models of disordered building blocks according to eqs. (1) and (3) with $\sigma_G = 10$ ($\sigma_G = 0.1$ for the top curve only). L index of $00L$ reflections in single phase epitaxial MBT films are indicated at the bottom, and substrate reflection at the top. ΔQ splitting of diffraction peaks $L6$ and $L18$ is proportional to the Mn deficit $\gamma = m/(n+m)$.

VI. CONCLUSION

X-ray diffraction simulation in $(\text{MnBi}_2\text{Te}_4)_n(\text{Bi}_2\text{Te}_3)_m$ structure models as a function of composition and disorder has pointed out a few features that can be promptly exploited in structural analysis of MBT films obtained by molecular beam epitaxy. There are diffraction peaks that split up into superlattice satellites peaks whose separation is directly proportional to the Mn deficit γ , and another peak whose position can be used to measure the value of γ . On top of this, there are peaks with line profiles independent of composition and disorder, and can lead to a measure of the longitudinal coherence length. The models used to demonstrate these features were based on a Gaussian probability distribution of the two building blocks present in the $n:m$ heterostructures. The experimental results showed

that increasing the Mn supply provides just a little improvement in composition, with x from around 0.7 to 0.8. The MBT phase with highest composition, $x = 0.86$, was observed in the thicker film where some phase segregation is also observed.

ACKNOWLEDGMENTS

We acknowledge financial support from the DFG through No. SFB1170 "Tocotronics" (Projects A01 and C06), No. SFB1143 "Correlated Magnetism," and the Würzburg-Dresden Cluster of Excellence on Complexity and Topology in Quantum Matter ct.qmat (EXC 2147, Project No.390858490) and from the BMBF (Project No. 05K19WW2). R.F.S.P., Y.G.C., and S.L.M. acknowledges financial support from FAPESP (Grant No. 2019/01946-1, 2019/11564-9), CNPq (Grant No. 310432/2020-0), and CAPES (finance code 001).

[1] M. M. Otrokov, I. P. Rusinov, M. Blanco-Rey, M. Hoffmann, A. Y. Vyazovskaya, S. V. Ereemeev, A. Ernst, P. M. Echenique, A. Arnau, and E. V. Chulkov, Unique thickness-dependent properties of the van der waals interlayer antiferromagnet mnbi_2te_4 films, *Phys. Rev. Lett.* **122**, 107202 (2019).

[2] W. Mortelmans, S. De Gendt, M. Heyns, and C. Merckling, Epitaxy of 2d chalcogenides: Aspects and consequences of weak van der waals coupling, *Appl. Mater. Today* **22**, 100975 (2021).

[3] H. Li, C. Li, B. Tao, S. Gu, Y. Xie, H. Wu, G. Zhang, G. Wang, W. Zhang, and H. Chang, Two-dimensional

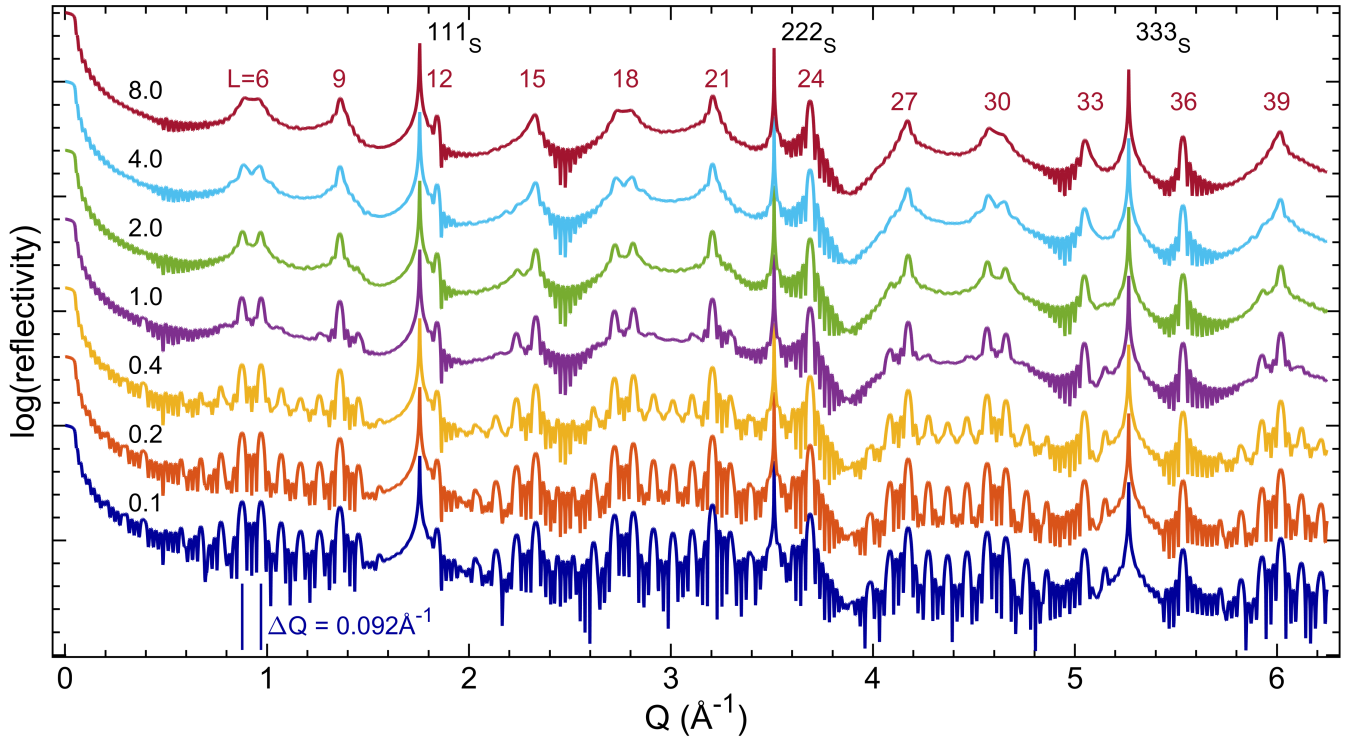


FIG. 8. Simulated Q -scans in epitaxial $(\text{MnBi}_2\text{Te}_4)_{16}(\text{Bi}_2\text{Te}_3)_4$ films on BaF_2 (111) substrate as a function of $\sigma_G = 0.1, 0.2, \dots, 8$ in eq. (3). Each simulation corresponds to the average curve calculated over an ensemble of 100 models of disordered heterostructures, such as those in Figure 3.

- metal telluride atomic crystals: Preparation, physical properties, and applications, *Adv. Funct. Mater.*, 2010901 (2021).
- [4] Y. L. Chen, J. G. Analytis, J.-H. Chu, Z. K. Liu, S.-K. Mo, X. L. Qi, H. J. Zhang, D. H. Lu, X. Dai, Z. Fang, S. C. Zhang, I. R. Fisher, Z. Hussain, and Z.-X. Shen, Experimental realization of a three-dimensional topological insulator, Bi_2Te_3 , *Science* **325**, 178 (2009).
- [5] H. Zhang, C.-X. Liu, X.-L. Qi, X. Dai, Z. Fang, and S.-C. Zhang, Topological insulators in Bi_2Se_3 , Bi_2Te_3 and Sb_2Te_3 with a single dirac cone on the surface, *Nat. Phys.* **5**, 438 (2009).
- [6] Y. Xia, D. Qian, D. Hsieh, L. Wray, A. Pal, H. Lin, A. Bansil, D. Grauer, Y. S. Hor, R. J. Cava, and M. Z. Hasan, Observation of a large-gap topological-insulator class with a single dirac cone on the surface, *Nat. Phys.* **5**, 398 (2009).
- [7] D. Hsieh, Y. Xia, D. Qian, L. Wray, F. Meier, J. H. Dil, J. Osterwalder, L. Patthey, A. V. Fedorov, H. Lin, A. Bansil, D. Grauer, Y. S. Hor, R. J. Cava, and M. Z. Hasan, Observation of time-reversal-protected single-dirac-cone topological-insulator states in Bi_2Te_3 and Sb_2Te_3 , *Phys. Rev. Lett.* **103**, 146401 (2009).
- [8] Y.-Y. Li, G. Wang, X.-G. Zhu, M.-H. Liu, C. Ye, X. Chen, Y.-Y. Wang, K. He, L.-L. Wang, X.-C. Ma, H.-J. Zhang, X. Dai, Z. Fang, X.-C. Xie, Y. Liu, X.-L. Qi, J.-F. Jia, S.-C. Zhang, and Q.-K. Xue, Intrinsic topological insulator Bi_2Te_3 thin films on Si and their thickness limit, *Adv. Mater.* **22**, 4002 (2010).
- [9] G. Wang, X.-G. Zhu, Y.-Y. Sun, Y.-Y. Li, T. Zhang, J. Wen, X. Chen, K. He, L.-L. Wang, X.-C. Ma, J.-F. Jia, S. B. Zhang, and Q.-K. Xue, Topological insulator thin films of Bi_2Te_3 with controlled electronic structure, *Adv. Mater.* **23**, 2929 (2011).
- [10] K. Hoefer, C. Becker, D. Rata, J. Swanson, P. Thalmeier, and L. H. Tjeng, Intrinsic conduction through topological surface states of insulating Bi_2Te_3 epitaxial thin films, *Proc. Natl. Acad. Sci. U.S.A.* **111**, 14979 (2014).
- [11] Y. Guo, Z. Liu, and H. Peng, A roadmap for controlled production of topological insulator nanostructures and thin films, *Small* **11**, 3290 (2015).
- [12] S. L. Morelhão, S. W. Kycia, S. Netzke, C. I. Fornari, P. H. O. Rappl, and E. Abramof, Dynamics of defects in van der Waals epitaxy of bismuth telluride topological insulators, *J. Phys. Chem. C* **123**, 24818 (2019).
- [13] C. I. Fornari, E. Abramof, P. H. O. Rappl, S. W. Kycia, and S. L. Morelhão, Morphology control in van der Waals epitaxy of bismuth telluride topological insulators, *MRS Advances* **5**, 1891 (2020).
- [14] C.-Z. Chang, J. Zhang, X. Feng, J. Shen, Z. Zhang, M. Guo, K. Li, Y. Ou, P. Wei, L.-L. Wang, Z.-Q. Ji, Y. Feng, S. Ji, X. Chen, J. Jia, X. Dai, Z. Fang, S.-C. Zhang, K. He, Y. Wang, L. Lu, X.-C. Ma, and Q.-K. Xue, Experimental observation of the quantum anomalous hall effect in a magnetic topological insulator, *Science* **340**, 167 (2013).
- [15] C.-Z. Chang, W. Zhao, D. Y. Kim, H. Zhang, B. A. As-saf, D. Heiman, S.-C. Zhang, C. Liu, M. H. W. Chan, and J. S. Moodera, High-precision realization of robust quantum anomalous hall state in a hard ferromagnetic topological insulator, *Nat. Mater.* **14**, 473 (2015).

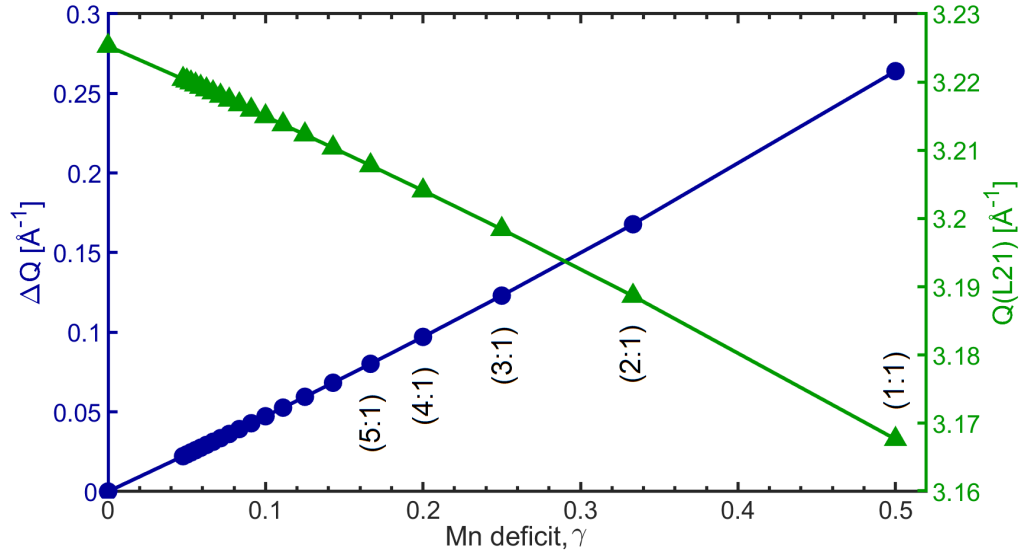


FIG. 9. Structural parameters accessible from X-ray reflectivity curves as a function of the Mn deficit γ in MBT films. ΔQ (blue solid line and circles, left axis) stands for the separation between adjacent superlattice peaks, eq. (6), that are well visible as a splitting of the $L6$ and $L18$ peaks. $Q(L21)$ (green solid line and triangles, right axis) is the $L21$ peak position given by eq. (7). $\gamma = m/(n + m)$ for a film with composition $n:m$ as indicated near a few points.

- [16] C. I. Fornari, H. Bentmann, S. L. Morelhão, T. R. F. Peixoto, P. H. O. Rappl, A.-V. Tcakaev, V. Zabolotnyy, M. Kamp, T.-L. Lee, C.-H. Min, P. Kagerer, R. C. Vidal, A. Isaeva, M. Ruck, V. Hinkov, F. Reinert, and E. Abramof, Incorporation of europium in bi_2te_3 topological insulator epitaxial films, *J. Phys. Chem. C* **124**, 16048 (2020).
- [17] A. I. Figueroa, S. E. Harrison, L. J. Collins-McIntyre, G. van der Laan, and T. Hesjedal, Magnetic ordering in ho-doped bi_2te_3 topological insulator, *Phys. Status Solidi RRL* **10**, 467 (2016).
- [18] S. E. Harrison, L. J. Collins-McIntyre, P. Schönherr, A. Vailionis, V. Srot, P. A. van Aken, A. J. Kellock, A. Pushp, S. S. P. Parkin, J. S. Harris, B. Zhou, Y. L. Chen, and T. Hesjedal, Massive dirac fermion observed in lanthanide-doped topological insulator thin films, *Sci. Rep.* **5**, 15767 (2015).
- [19] M. M. Otrokov, I. I. Klimovskikh, H. Bentmann, D. Estyunin, A. Zeugner, Z. S. Aliev, S. Gaß, A. U. B. Wolter, A. V. Koroleva, A. M. Shikin, M. Blanco-Rey, M. Hoffmann, I. P. Rusinov, A. Y. Vyazovskaya, S. V. Ere-meev, Y. M. Koroteev, V. M. Kuznetsov, F. Freyse, J. Sánchez-Barriga, I. R. Amiraslanov, M. B. Babanly, N. T. Mamedov, N. A. Abdullayev, V. N. Zverev, A. Al-fonsov, V. Kataev, B. Büchner, E. F. Schwier, S. Kumar, A. Kimura, L. Petaccia, G. Di Santo, R. C. Vidal, S. Schatz, K. Kießner, M. ünzelmann, C. H. Min, S. Moser, T. R. F. Peixoto, F. Reinert, A. Ernst, P. M. Echenique, A. Isaeva, and E. V. Chulkov, Prediction and observation of an antiferromagnetic topological insulator, *Nature* **576**, 416 (2019).
- [20] J. Li, Y. Li, S. Du, Z. Wang, B.-L. Gu, S.-C. Zhang, K. He, W. Duan, and Y. Xu, Intrinsic magnetic topological insulators in van der waals layered mnbi_2te_4 -family materials, *Sci. Adv.* **5**, 10.1126/sciadv.aaw5685 (2019).
- [21] J. W. G. Bos, H. W. Zandbergen, M.-H. Lee, N. P. Ong, and R. J. Cava, Structures and thermoelectric properties of the infinitely adaptive series $(\text{Bi}_2)_m(\text{Bi}_2\text{Te}_3)_n$, *Phys. Rev. B* **75**, 195203 (2007).
- [22] C. I. Fornari, P. H. O. Rappl, S. L. Morelhão, and E. Abramof, Structural properties of Bi_2Te_3 topological insulator thin films grown by molecular beam epitaxy on (111) BaF_2 substrates, *J. Appl. Phys.* **119**, 165303 (2016).
- [23] H. Steiner, V. Volobuev, O. Caha, G. Bauer, G. Springholz, and V. Holý, Structure and composition of bismuth telluride topological insulators grown by molecular beam epitaxy, *J. Appl. Cryst.* **47**, 1889 (2014).
- [24] Z. S. Aliev, I. R. Amiraslanov, D. I. Nasonova, A. V. Shevelkov, N. A. Abdullayev, Z. A. Jahangirli, E. N. Orujlu, M. M. Otrokov, N. T. Mamedov, M. B. Babanly, and E. V. Chulkov, Novel ternary layered manganese bismuth tellurides of the mn_2te_3 system: Synthesis and crystal structure, *J. Alloys Compd.* **789**, 443 (2019).
- [25] P. Kagerer, C. I. Fornari, S. Buchberger, S. L. Morelhão, R. C. Vidal, A. Tcakaev, V. Zabolotnyy, E. Weschke, V. Hinkov, M. Kamp, B. Büchner, A. Isaeva, H. Bentmann, and F. Reinert, Molecular beam epitaxy of antiferromagnetic $(\text{mnbi}_2\text{te}_4)(\text{bi}_2\text{te}_3)$ thin films on baf_2 (111), *J. Appl. Phys.* **128**, 135303 (2020).
- [26] E. D. L. Rienks, S. Wimmer, J. Sánchez-Barriga, O. Caha, P. S. Mandal, J. Růžicka, A. Ney, H. Steiner, V. V. Volobuev, H. Groiss, M. Albu, G. Kothleitner, J. Michalička, S. A. Khan, J. Minár, H. Ebert, G. Bauer, F. Freyse, A. Varykhalov, O. Rader, and G. Springholz, Large magnetic gap at the dirac point in $\text{bi}_2\text{te}_3/\text{mnbi}_2\text{te}_4$ heterostructures, *Nature* **576**, 423 (2019).
- [27] R. C. Vidal, A. Zeugner, J. I. Facio, R. Ray, M. H. Haghighi, A. U. B. Wolter, L. T. Corredor Bohorquez, F. Cagliaris, S. Moser, T. Figgemeier, T. R. F. Peixoto, H. B. Vasili, M. Valvidares, S. Jung, C. Cacho, A. Al-

- fonsov, K. Mehlatat, V. Kataev, C. Hess, M. Richter, B. Büchner, J. van den Brink, M. Ruck, F. Reinert, H. Bentmann, and A. Isaeva, Topological electronic structure and intrinsic magnetization in mnbi_4te_7 : A bi_2te_3 derivative with a periodic mn sublattice, *Phys. Rev. X* **9**, 041065 (2019).
- [28] S. L. Morelhão, G. E. S. Brito, and E. Abramof, Nanos-structure of sol-gel films by x-ray specular reflectivity, *Appl. Phys. Lett.* **80**, 407 (2002).
- [29] S. L. Morelhão, C. I. Fornari, P. H. O. Rappl, and E. Abramof, Nanoscale characterization of bismuth telluride epitaxial layers by advanced x-ray analysis, *J. Appl. Cryst.* **50**, 399 (2017).
- [30] S. L. Morelhão, C. M. R. Remédios, R. O. Freitas, and A. O. dos Santos, X-ray phase measurements as a probe of small structural changes in doped nonlinear optical crystals, *J. Appl. Cryst.* **44**, 93 (2011).
- [31] A. Antunes, A. M. V. Safatle, P. S. M. Barros, and S. L. Morelhão, X-ray imaging in advanced studies of ophthalmic diseases, *Med. Phys.* **33**, 2338 (2006).
- [32] A. K. Geim and I. V. Grigorieva, Van der waals heterostructures, *Nature* **499**, 419 (2013).
- [33] P. A. Vermeulen, J. Mulder, J. Momand, and B. J. Kooi, Strain engineering of van der waals heterostructures, *Nanoscale* **10**, 1474 (2018).
- [34] J. A. Hagmann, X. Li, S. Chowdhury, S.-N. Dong, S. Rouvimov, S. J. Pookpanratana, K. M. Yu, T. A. Orlova, T. B. Bolin, C. U. Segre, D. G. Seiler, C. A. Richter, X. Liu, M. Dobrowolska, and J. K. Furdyna, Molecular beam epitaxy growth and structure of self-assembled $\text{bi}_2\text{se}_3/\text{bi}_2\text{mnse}_4$ multilayer heterostructures, *New J. Phys.* **19**, 085002 (2017).
- [35] G. Springholz, S. Wimmer, H. Groiss, M. Albu, F. Hofer, O. Caha, D. Kriegner, J. Stangl, G. Bauer, and V. Holý, Structural disorder of natural bi_mse_n superlattices grown by molecular beam epitaxy, *Phys. Rev. Materials* **2**, 054202 (2018).
- [36] M. Idrees, H. U. Din, S. A. Khan, I. Ahmad, L.-Y. Gan, C. V. Nguyen, and B. Amin, Van der waals heterostructures of p, bse, and sic monolayers, *Journal of Applied Physics* **125**, 094301 (2019).
- [37] S. L. Morelhão and S. Kycia, Enhanced x-ray phase determination by three-beam diffraction, *Phys. Rev. Lett.* **89**, 015501 (2002).
- [38] D. S. Lee, T.-H. Kim, C.-H. Park, C.-Y. Chung, Y. S. Lim, W.-S. Seo, and H.-H. Park, Crystal structure, properties and nanostructuring of a new layered chalcogenide semiconductor, $\text{bi}_2\text{mn}_2\text{te}_4$, *CrystEngComm* **15**, 5532 (2013).
- [39] S. Nakajima, The crystal structure of $\text{bi}_2\text{te}_{3-x}\text{se}_x$, *J. Phys. Chem. Solids* **24**, 479 (1963).
- [40] N. Bouad, L. Chapon, R.-M. Marin-Ayral, F. Bouree-Vigner, and J.-C. Tedenac, Neutron powder diffraction study of strain and crystallite size in mechanically alloyed pbte, *J. Solid State Chem.* **173**, 189 (2003).
- [41] H. Franzen and C. Sterner, The x-ray photoelectron spectra of mns, mnse, and mn₂te, *J. Solid State Chem.* **25**, 227 (1978).
- [42] J.-Q. Yan, Q. Zhang, T. Heitmann, Z. Huang, K. Y. Chen, J.-G. Cheng, W. Wu, D. Vaknin, B. C. Sales, and R. J. McQueeney, Crystal growth and magnetic structure of mnbi_2te_4 , *Phys. Rev. Materials* **3**, 064202 (2019).
- [43] T. Hirahara, M. M. Otrokov, T. T. Sasaki, K. Sumida, Y. Tomohiro, S. Kusaka, Y. Okuyama, S. Ichinokura, M. Kobayashi, Y. Takeda, K. Amemiya, T. Shirasawa, S. Ideta, K. Miyamoto, K. Tanaka, S. Kuroda, T. Okuda, K. Hono, S. V. Eremeev, and E. V. Chulkov, Fabrication of a novel magnetic topological heterostructure and temperature evolution of its massive dirac cone, *Nature Communications*, 4821 (2020).
- [44] S. L. Morelhão, S. Kycia, S. Netzke, C. I. Fornari, P. H. O. Rappl, and E. Abramof, Hybrid reflections from multiple x-ray scattering in epitaxial bismuth telluride topological insulator films, *Appl. Phys. Lett.* **112**, 101903 (2018).
- [45] T. P. Ginley, Y. Wang, and S. Law, Topological insulator film growth by molecular beam epitaxy: A review, *Crystals* **6**, 154 (2016).
- [46] L. A. Walsh and C. L. Hinkle, van der waals epitaxy: 2d materials and topological insulators, *Applied Materials Today* **9**, 504 (2017).
- [47] A. Ghasemi, D. Kepaptsoglou, P. L. Galindo, Q. M. Ramasse, T. Hesjedal, and V. K. Lazarov, Van der waals epitaxy between the highly lattice mismatched cu-doped fese and bi_2te_3 , *NPG Asia Materials*, e402 (2017).